PERGAMON

Journal of Structural Geology 22 (2000) 1569–1579

JOURNAL OF STRUCTURAL GEOLOGY

www.elsevier.nl/locate/jstrugeo

Automated grain boundary detection and classification in orientation contrast images

M. Bartozzi*, A.P. Boyle, D.J. Prior

Department of Earth Sciences, Liverpool University, Liverpool L69 3BX, UK

Received 30 November 1999; accepted 29 June 2000

Abstract

An unbiased and unequivocally defined estimate of grain sizes and shapes is fundamental for understanding the microscopic behaviour of crystalline materials modified by the action of stress fields and/or chemical gradients. Because of their very good spatial resolution, orientation contrast (OC) images represent a useful starting point to develop an automated technique able to assess grain boundaries in a completely objective and reproducible way. The method presented in this contribution defines boundaries as high brightness gradient features on an OC image of a quartz mylonite through a specifically designed sequence of detection and filter algorithms that minimise the effect of local background noise. The object set into which the OC image has been divided is further analysed to compute a set of positions where to perform electron backscatering diffraction analysis and build a crystal orientation data set. This data set is then used along with information from the detection-filtering algorithm to automatically rebuild the real grain boundary net. The obtained results are in good agreement with results from similar manual techniques, while the whole determination process is also much faster than other automated electron backscattering diffraction analytical methods.

1. Introduction

Backscattered electrons (BSE) are one of the many products of the interaction between high energy electrons and matter that is at the basis of the Scanning Electron Microscopy (SEM; Newbury et al., 1986; Reimer, 1985; Lloyd, 1987). The number of BSE, or signal intensity, yielded by the incidence area depends on:

- the incident beam current;
- the energy of the incident electrons;
- the angle between the incidence direction and the normal to the sample surface;
- the average atomic number of the sample material in the considered unit area;
- the crystal lattice orientation with respect to a sample fixed reference frame.

Moreover, the signal intensity is not isotropically distributed around the incidence area, but also depends on the BSE detector direction. The analogue signal intensity can be coded as a number and stored in digital form. If this operation is performed on a two-dimensional matrix of evenly distributed incidence areas, it is possible to represent the sample surface as a digital image, in which a pixel corresponds to an incidence area and its grey level to the signal intensity detected from that area.

The grey scale image varies with the type and geometry of the image acquisition system and the SEM operating conditions. For instance, with the electron beam perpendicular to the sample surface, an image taken from a 90° angle (i.e. the beam direction) bears information related to the average atomic number of the imaged material. The technique is known as backscatter or *z*-contrast imaging. While *z*-contrast images are very useful to identify phases of different chemical composition, minerals of the same mean atomic number have the same grey level. Boundaries between grains of the same phase are difficult to recognise.

This paper considers the case in which the incident direction is not perpendicular to the sample surface and the signal intensity is measured at a low angle from the sample surface. Under these conditions the signal intensity is predominantly related to the crystal lattice orientation in the incidence area as a result of electron channelling (EC) effects that occur inside the sample. Images obtained from this kind of signal are known as orientation contrast (OC) images, in which grey level contrast reflects changes in crystal lattice orientation and therefore allows the identification of crystal domain boundaries.

* Corresponding author.
E-mail address: zaphod@liverpool.ac.uk (M. Bartozzi).

0191-8141/00/$ - see front matter
PII: S0191-8141(00)00084-5

Electron backscattered diffraction (EBSD) can be used to identify the orientation of the crystal lattice domain in the incidence area, relative to a chosen reference system. According to Euler's theorem on the motion of rigid bodies (Goldstein, 1980), it is always possible to make one coordinate system coincident with another by a single rotation around a rotation axis. Therefore, the orientation of a domain can be described relative to the orientation of another domain as an angle/axis pair following the Euler's theorem statement. The rotation angle is known in microstructure analysis as the misorientation angle, and the rotation axis as the misorientation axis. The axis/angle pair is only unique in the absence of crystal symmetries. In the case of quartz (point symmetry 32) there are six equivalent axis/angle pairs, of which the one with the minimum rotation angle is conventionally chosen. A boundary between two domains identified on an OC image can be characterised by the misorientation angle between the two domains. Boundaries can be classified accordingly and a hierarchy can be tentatively established that allows domains to be interpreted as grains or subgrains of different orders.

An automated technique known as automated crystal orientation mapping (ACOM) allows the definition of grain boundary maps by performing EBSD analysis on an array of points evenly distributed on a sample (Adams, 1997; Adams et al., 1993, 1994; Kunze et al., 1995). To obtain the maximum possible precision in locating boundaries, ACOM analyses need to be done at the smallest intervals allowed by the system spatial resolution. Thus, for a spatial resolution of 1 μm (as for the case presented here), ACOM analysis of a 1 mm^2 area would require up to 2.5×10^5 individual EBSD analyses. While ACOM use in metallurgy is common, it presents many problems with geological samples, of which the three most important are:

- pseudosymmetry, that makes automated definition of crystal lattice orientation unreliable for low symmetry minerals like quartz or feldspars;
- long operational times, that magnify the charging effect typical of poorly conductive materials, resulting in a progressive deterioration in the quality of EBSD results and in sample surface physical damage;
- charging, which limits the spatial resolution of any EBSD techniques, as the incident beam may be deflected from the position where it was directed to.

An alternative approach is to use an OC image of the sample to identify crystallographic domains, and then use EBSD analysis on relevant positions only, effectively reducing operational time. Currently, this is a manual task that requires a great human effort in terms of time to identify objects, digitise domain boundaries and decide the position of any single point to be analysed. Because the brightness contrast between two adjacent domains can be very poor, the position or even the existence of a boundary becomes necessarily subjective, affecting the significance of any subsequent analysis. In this paper a newly developed procedure is presented that provides an automated grain boundary definition by the application of image analysis techniques on OC images. A short description of the program is given, and the results of its application on a small area of a quartz mylonite sample are analysed and compared with EBSD data obtained from the same sample area.

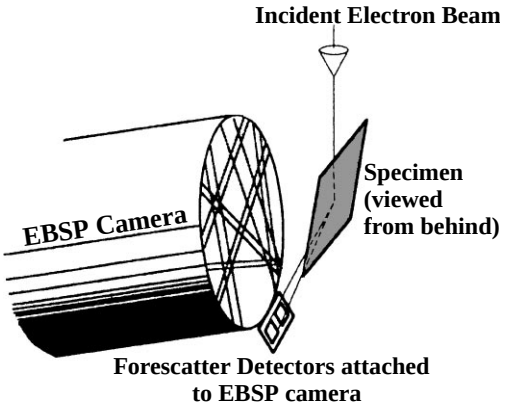

Fig. 1. Schematic representation of the SEM internal chamber set up for OC images collection. The specimen is tilted to 70° with respect to the electron beam direction, and the forescatter sensors set is mounted forward of the specimen (modified from Prior et al., 1996).

2. Techniques

The sample studied is a quartz mylonite prepared as a standard polished thin section (30 μm thick), which was then polished using a SYTON chemical–mechanical method in order to remove surface damage. A fine (<5 nm) carbon coating has been applied to reduce the effects of charging during SEM analyses and the thin-section edges were coated with conductive carbon paint and connected to earth through the sample holder (Trimby and Prior, 1999).

Both OC imaging and EBSD analysis have been carried out using a Philips XL30 SEM with a tungsten filament electron gun. The sample has been tilted to form a 70° angle between its normal and the incident direction. A set of two semiconductor sensors mounted forward of the sample and under the EBSD camera has been used to collect the EC electron flow (Fig. 1). The sensors are connected to a manually operated amplifier whose analog output signal (formed by summing together the two sensor signals in order to reduce background noise) is then hardware converted into a digital form and displayed on a computer screen as an OC image. OC images obtained from sensors mounted forward of the sample are also referred to as Forescatter images. In the following text, the term OC will be used, but in this case is used synonymously with Forescatter.

The SEM experimental conditions for this study required

a considered choice of SEM settings for both OC imaging and EBSD, especially because the carbon coat tends to reduce the signal quality with respect to uncoated samples. (Trimby, 1998; Prior and Wheeler, 1999). For OC imaging the working distance (WD) was 23.5 mm and the accelerating voltage (AccV) was 25 kV. The spot size (Sp) refers to codes used by the Philips operating system, in which, at AccV = 20 kV and WD = 20 mm, the correspondences between Sp and beam currents are approximately: Sp5 = 0.8 nA, Sp6 = 3.2 nA, Sp7 = 13.2 nA (Prior and Wheeler, 1999). Under the operating conditions described above, Sp 5.6 has been used. An AccV of 20 kV has also been tried. The resultant OC image was characterised by low overall contrast at any Sp value, with many domains being indistinguishable. With AccV = 25 kV, the useful Sp interval proved to be very narrow, ranging from Sp5.5 to Sp5.7 (respectively, 2.5 and 3.1 nA). Sp values outside this range again gave very poor contrast images. Changes in activation volume shape and depth beneath the coated sample surface might constitute a possible reason for these effects. In order to avoid any modification of the system geometry (to which OC imaging is very sensitive) the sample remained in the SEM chamber throughout the entire experiment.

The scan rate has been set at 240 ms per line and 1936 scan lines per frame, for a total scan time of 7 min 5 s to obtain an improved signal-to-noise ratio, and therefore reduce gaussian noise intensity in the resultant OC image, which is shown in Fig. 2a. Its dimension is 712×484 pixels (standard output), which corresponds to 284.8×193.6 μm, each pixel being 0.4 μm in length, or 0.16 μm^2 as covered area. Overall image brightness and contrast were optimised manually before acquisition to guarantee that brightness values of all its relevant parts stretch on the entire grey level scale. Some non-relevant features, like holes, hole rims and particles, have been set out of scale (either black or white). It has to be noted that not all the possible greyscale values are used in the image, because of the way in which the signal is converted from analog to digital by the Philips XL30 system. The number of used values is only 64 (6-bit image depth), instead of the available 256 (8-bit scale).

EBSD analysis has been performed on electron backscattered patterns (EBSP, Day, 1993; Kunze et al., 1995; Lloyd, 1987; Prior et al., 1996; Randle, 1992; Trimby, 1998; Trimby and Prior, 1999; Wilkinson and Hirsch, 1997) recorded on a phosphor screen and imaged using a low light TV camera (Trimby and Prior, 1999). CHANNEL + (v. 3.0) program, developed by HKL Software, was used to interpret EBSPs in terms of crystallographic orientations stored as sets of Euler angles for each measured indexable EBSD pattern. SEM conditions for EBSD operations were AccV = 25 kV, WD = 23.5 mm, Sp7 (for a beam current correspondent to ≈ 16 nA).

The spatial resolution for both OC imaging and EBSD analysis is approximately 1 μm. The angular resolution is $<1°$ for OC imaging and approximately 1° for EBSD.

3. Program description

The computer procedure evaluates brightness gradient distributions in the image and then attempts to define boundaries from these. These boundaries are subsequently skeletonised, and then rebuilt to make a complete boundary map. Some details of these procedures are given below, and a complete description of the technique can be found in a web page at the Internet address: www.pcweb.liv.ac.uk/apboyle/bartozzi

3.1. Gradient-based boundary pixel definition

Brightness change is evaluated with reference to a square area (kernel). The new algorithm reported here analyses brightness gradients along all possible radial directions in the kernel. The final brightness change value given to the kernel's central pixel is the standard deviation from the average of the population of linear gradients. Pixels on the boundary between areas with different brightness have high values, while pixels inside constant brightness areas will typically have low values. The algorithm also ensures that the value is not affected by local variations in background noise. The number of linear gradients required is limited by the kernel dimension. The following discussion will refer to 3×3 kernels, for each of which four linear gradients are calculated, at a 45° angular step. The entire data set is shown in Fig. 2b, rescaled to a grey level image.

3.2. Thresholding

The discrimination between boundary ('high value') and non-boundary ('low value') pixels is based on the shape of the frequency distribution curve obtained from the data set. Thus, the threshold value is optimised for any particular image rather than using a given fixed value. Nonetheless, as for any other threshold definition method, two main error sources are introduced: (a) a number of boundary pixels are classified as non-boundary type; (b) some non-boundary pixels are classified as boundary type.

Both error types are due to the lack of a sharp difference between some of the image domains. In these cases, even if a large-scale brightness change exists, borders between domains are masked by random noise. Results can comprise missing boundaries, false boundaries, creation of small false objects isolated or in chains along the real boundary, and misplaced boundaries.

The boundary pixels subset for the example image is shown in Fig. 2c.

3.3. Skeletonisation and fragmentation

Domains of contiguous boundary pixels need to be reduced to one-pixel wide boundary fragments (BFs). This task is performed by deleting pixels beginning with the smallest brightness change, which will minimise the loss of pixels coincident with real boundaries.

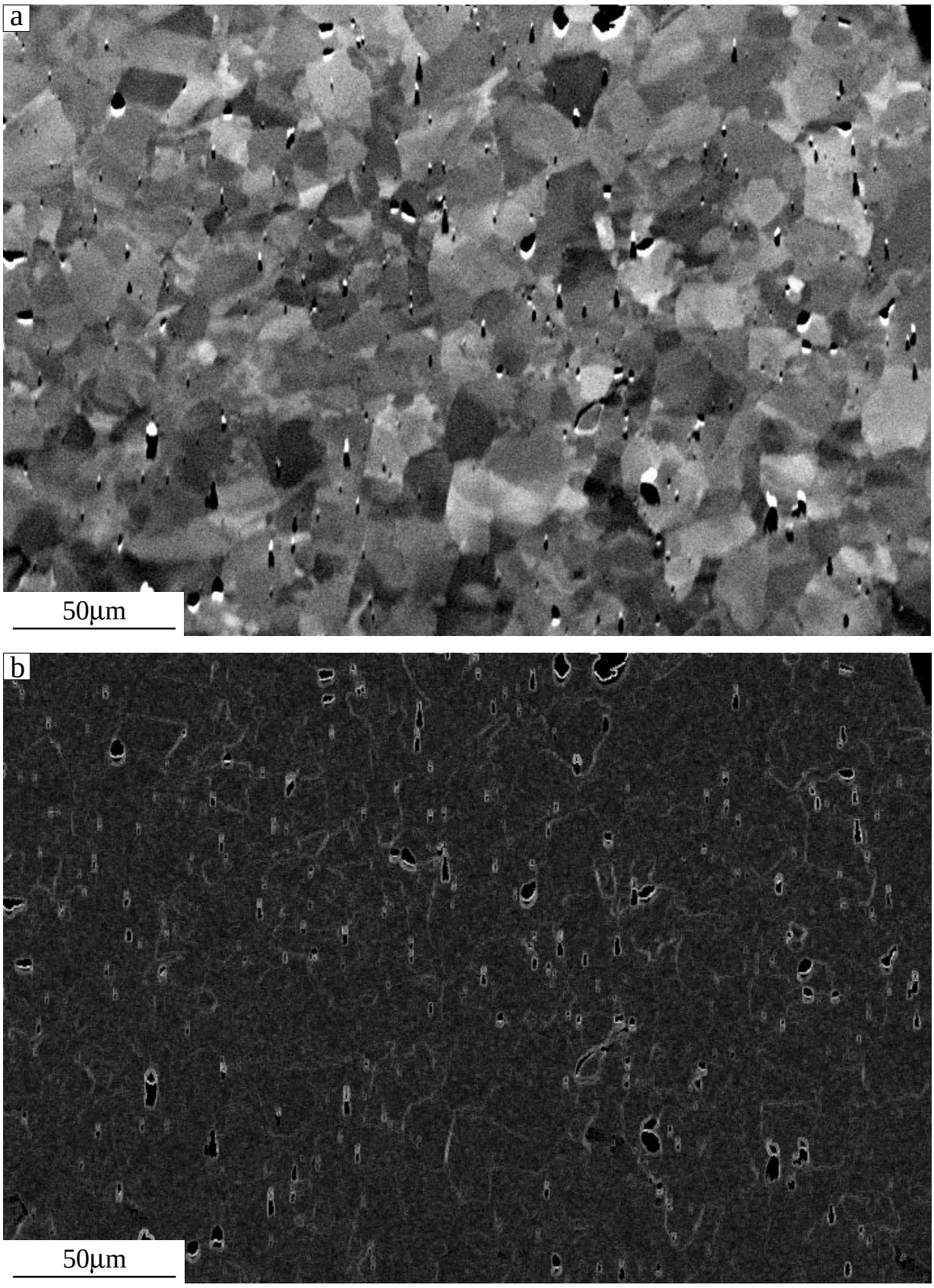

Fig. 2. (a) OC image of a quartz mylonite. (b) Grey level representation of brightness gradient distribution (white = high gradient). (c) Superimposition on the original image of the pixels with gradient higher than threshold. (d) Superimposition on the original image of the complete set of rebuilt BFs.

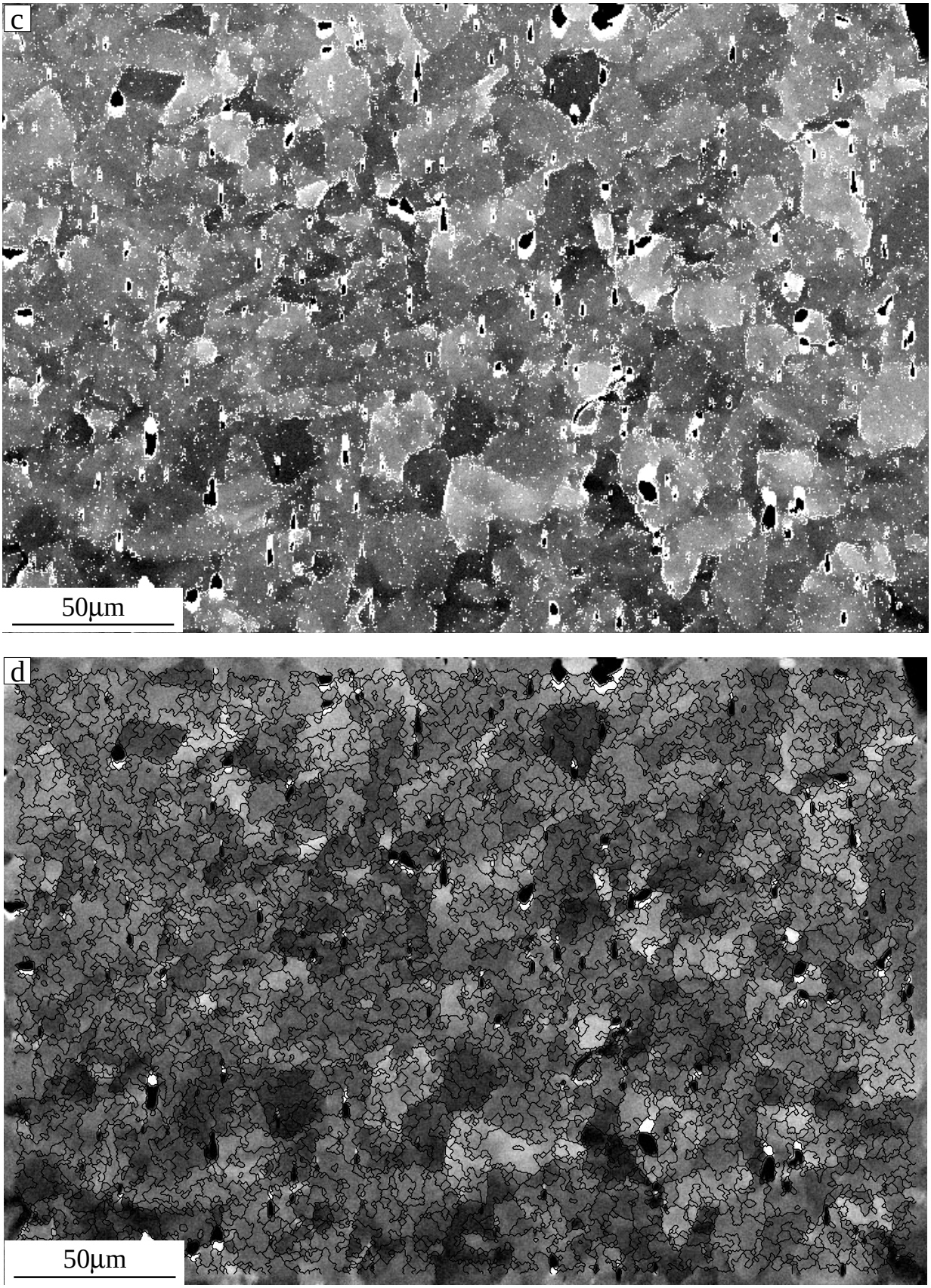

Fig. 2. (*continued*)

3.4. Rebuilding

The remaining BFs after skeletonisation are finally rebuilt and reconnected to form an uninterrupted boundary net (Fig. 2d). The rebuilding algorithm extends all the BFs from their endpoints following paths that maximise their average brightness change value. All the possible paths of given length are examined from any BF endpoint. The path length is manually defined by the operator. The number of examined paths increases exponentially with length, resulting in a dramatic increase in calculation time that is often not justified by a corresponding improvement in the result. Generally a length of six pixels has proved to be a reasonable compromise between results quality and execution time. This value has been used in the analysis presented here.

4. Results

An image of the kind considered here, can normally be automatically divided into thousands of objects. For the particular image shown in Fig. 2d, 4695 objects are defined by a boundary net comprising 13588 BFs. Because of the great complexity of the entire data set, only a small area will be used in the following discussion. The area (Fig. 3a) is 320×120 pixels wide, i.e. 128×48 μm, corresponding to the top-left eighth of the whole image. Unless stated otherwise, data refer to this area only. The data subset comprises 549 objects and 1590 BFs. There is no difference in shape between the gradient frequency distributions of the whole OC image and the considered area, as the latter is a representative sample of the former. The threshold position is therefore unchanged.

4.1. Visual appearance

While it can be stated that in the vast majority of cases the rebuilt boundaries visually correspond to real limits between objects, there is also a number of both false and missing boundaries. False boundaries have the effect of splitting some objects and creating some smaller false ones, while missing boundaries are the reason for the presence of clusters of unresolved objects (Fig. 3a). Both false and missing boundaries originate from the thresholding problems exposed in Section 3.2, as well as the objective difficulty of discerning between low average gradient BFs and background noise. It is, in principle, possible to implement better and far more complex boundary detection procedures. However, if extensively applied to the entire image they would result in unacceptable calculation times.

4.2. Average gradient-based classification

As BFs are associated with an average gradient value, it is possible to classify them accordingly. It is evident (Fig. 3b) that the spatial distribution of high-gradient BFs is not random but controlled by the presence of domains with roughly constant brightness. BFs with intermediate average gradient (Fig. 3c) partially follow the same pattern, but a consistent number of them are scattered inside the domains, either outlining low contrast limits between what may be defined as subdomains or simply cutting through areas of constant brightness (background noise excluded). Low-gradient BFs are evenly distributed across the entire image (Fig. 3d), and are clearly related to random fluctuations in background noise.

5. EBSD point analysis definition

While not all BFs can be considered as the real boundaries between crystal lattice domains of different orientation, they can be used as a reference guide to establish a list of point analysis co-ordinates on the image that can be fed to automatic EBSD analysis software. Three different situations with different analytical solutions can occur.

Situation 1: small objects, for which it would be impossible to define two or more point analysis whose distance from the closest portion of boundary and between them is less than two times the minimum spatial resolution.

Solution: one single point analysis coincident with object centroid.

Situation 2: medium and large objects with irregular shape.

Solution: one point analysis at the centroid of any significant protuberance and one at the centre of the main part of the object (if any). Shape based subdivision can successfully substitute gradient techniques in the case of contiguous objects with different lattice orientations but undifferentiated on OC image.

Situation 3: medium and large objects with irregular internal brightness distribution

Solution: they can be analysed using a far more complex method than the one applied on the entire OC image. If homogeneous subareas can be identified, a point analysis is placed at the subarea centroids.

A set of point analyses has been defined following the three rules mentioned above. The positions of the 468 of them for which EBSD indexing has been possible is shown in Fig. 4.

Fig. 3. (a) OC image portion used for the discussion and related BFs subset. Arrows point to a BF cutting through a uniform brightness area (α, 'false' BF), and to a missing BF (β). (b) BFs with average gradient gradient > 80 (gradient range scaled to 0–100). Their spatial distribution is clearly controlled by brightness changes. (c) BFs with average gradient $70 <$gradient < 80. Spatial distribution is still controlled by brightness changes, though a random component is also present. (d) BFs with average gradient gradient < 70. Spatial distribution is almost completely random and controlled by background noise.

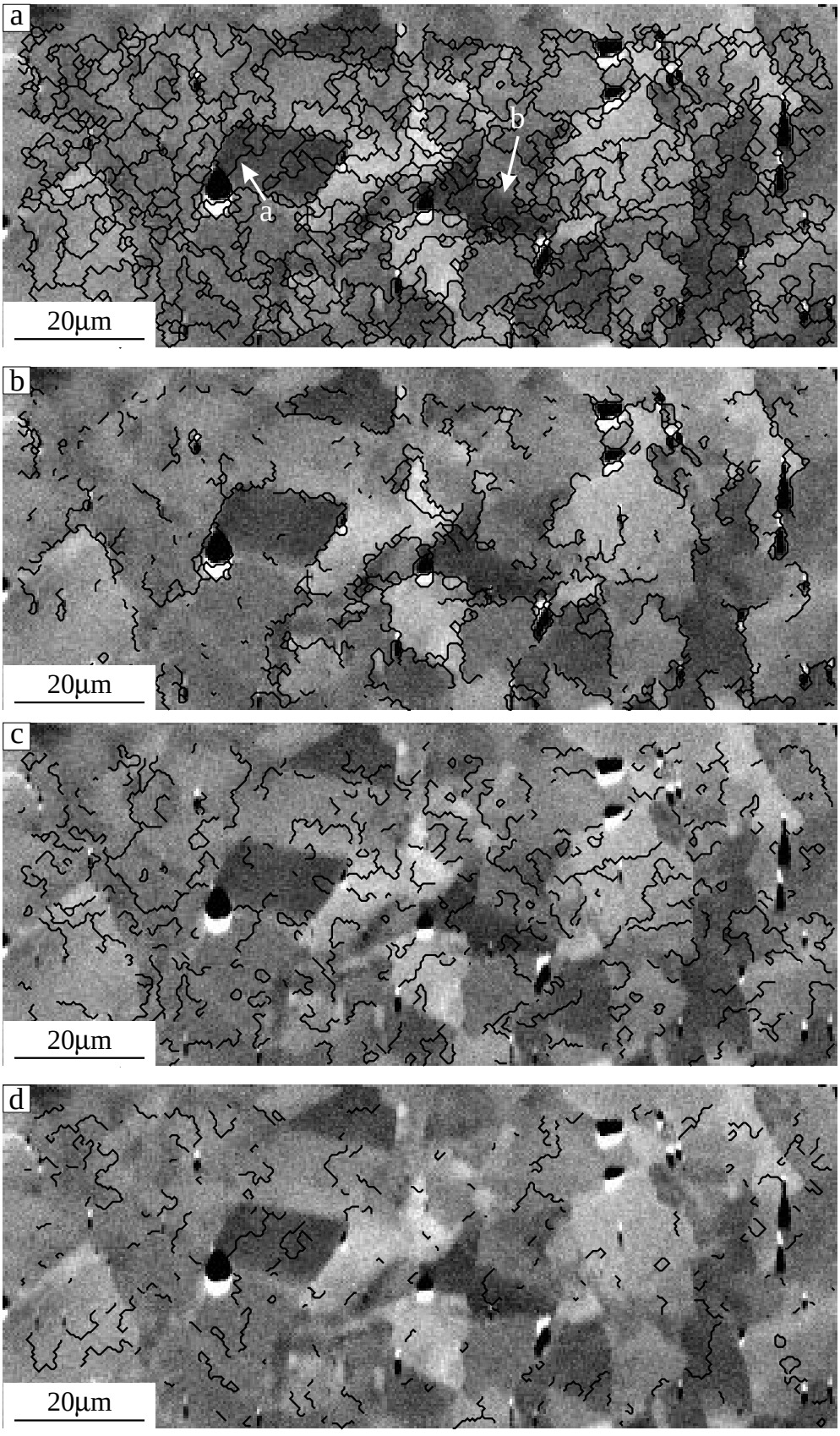
a
b
a
20µm
b
20µm
c
20µm
d
20µm

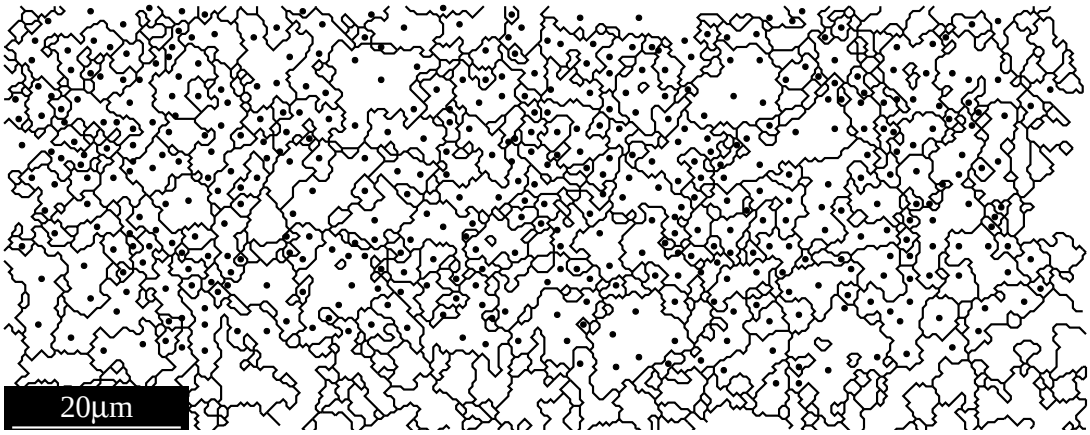

Fig. 4. Position of the 468 EBSD point analysis for which indexing has been possible.

After EBSD analysis, misorientation data are computed between pairs of points centred in contiguous objects or subareas. Occasionally, misorientation is manually computed between non-contiguous subareas if these are separated by an object for which EBSD indexing was not possible (including holes). The situation is schematised in Fig. 5.

Boundary fragments between objects found to have the same crystal lattice orientation are redefined on the basis of the misorientation data set. The new BFs can be of three different types.

- BFs automatically defined before EBSD analysis (the vast majority).
- Boundaries between subareas inside automatically defined objects, traced according to the three rules used to define point analysis positions.
- BFs cutting through non-indexed objects or subareas if no other option is available. In this case BF shape and position are estimated from shape and position of the surrounding BFs. This operation currently needs to be performed manually.

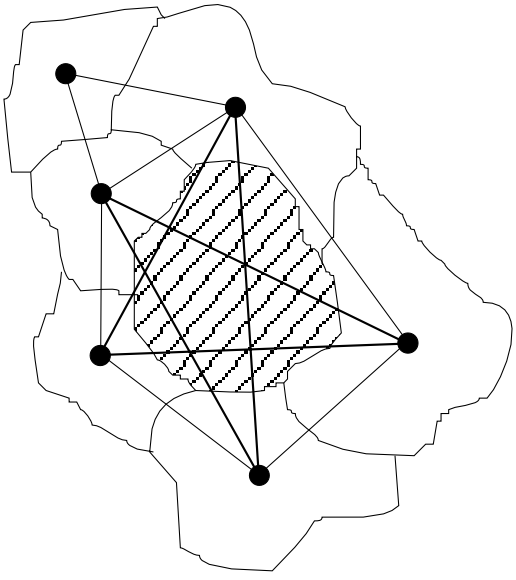

Fig. 5. When objects are separated by a non-indexed object or a hole (hatched object), all the possible pairs of non-adjacent objects that share a BF with it are manually evaluated (thick tie lines). The obtained misorientation data, along with the automatically obtained for the other object pairs (thin tie lines), are used to estimate a possible presence of a BF in correspondence of the unindexed object.

The entire set of post-EBSD boundaries is shown in Fig. 6a. Any boundary separates a pair of EBSD point analyses, and can be classified according to the misorientation angle computed for the pair.

6. Discussion

A number of considerations is suggested by the characteristics of the boundary set.

- BFs are hierarchically organised, as BFs of lower misorientation classes tend to be interrupted by BFs of higher classes. High misorientation class BFs tend to be continuous and interconnected.
- In the highest misorientation class ($\theta > 10°$), BFs are generally interconnected to define domains that can be interpreted as 'grains'. When interconnection does not occur (arrow in Fig. 6b) the reason is in most cases that the non-connected BF misorientation is close to the class lower limit, while the subsequent BF misorientation is just below the limit and thus assigned to the following class ($5° < \theta < 10°$). BFs' classification cannot be based only upon misorientation values, but it has to consider spatial continuity criteria. The same problem affects lower misorientation BF classes, but is masked by their natural fragmentation.
- BFs of the lowest misorientation class ($\theta < 1°$) do not fit into the hierarchical interpretation, as their misorientation value is lower than the 1° angular resolution instrumental limit for the SEM machine used. They need to be interpreted as non-existent boundaries generated either by

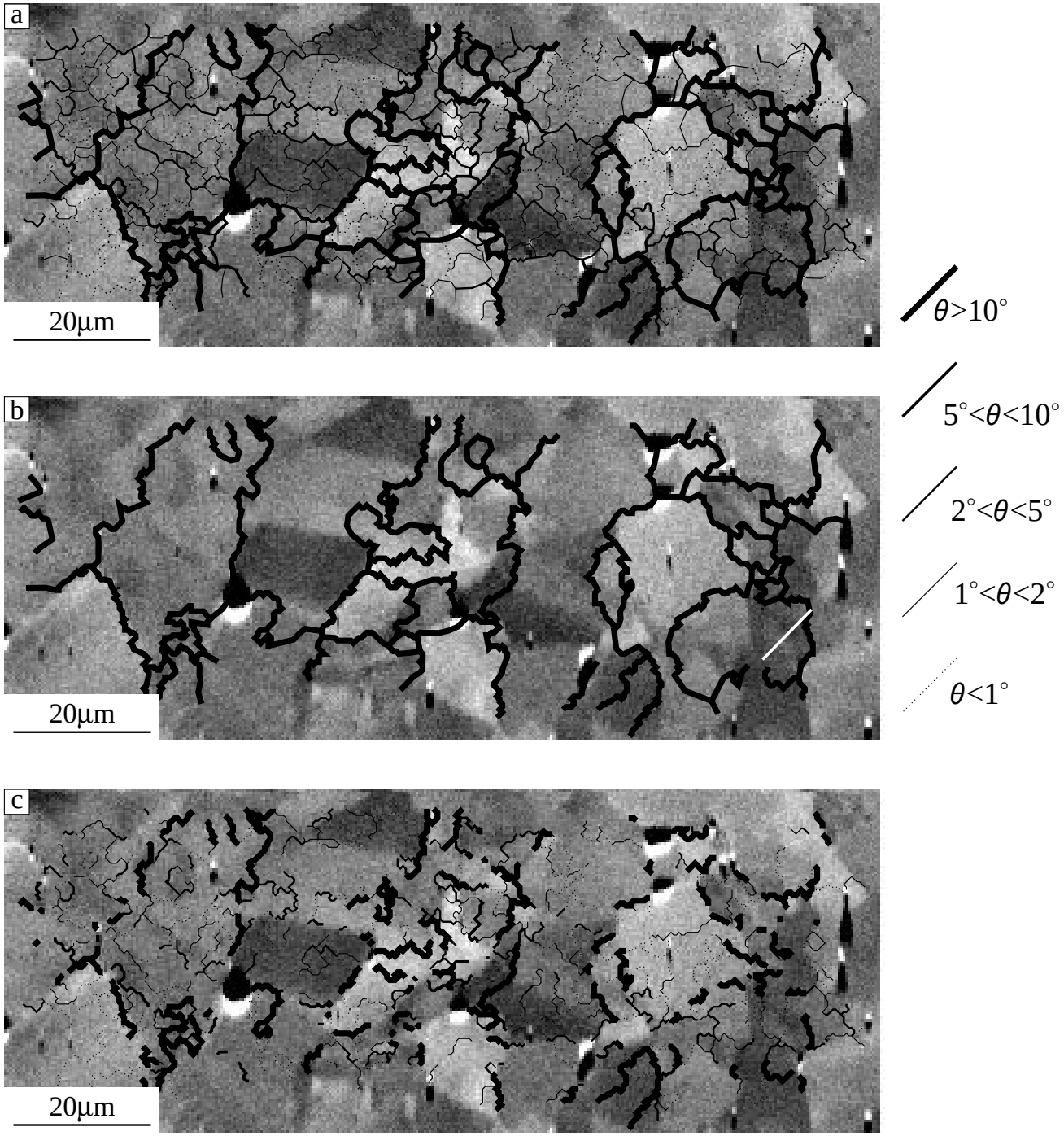

Fig. 6. (a) Boundary fragments obtained from EBSD and misorientation analysis. The BFs are classified according to the misorientation value for the point analysis pair from which the BF has been obtained. (b) BFs associated with misorientation $\theta > 10°$. In many cases there is no evident correlation between BFs distribution and brightness gradient of the OC image. BFs of this class are characterised by high interconnectedness, with exceptions where θ is close to the class lower limit (arrow). The missing link is assigned to the lower misorientation class ($5° < \theta < 10°$) as its misorienation value is just below the 10° threshold. (c) Post-EBSD BFs subset coincident with automatically defined BFs.

redundant EBSD data or by 'false' boundaries in the OC image. It is possible that some of them actually correspond to real low angle boundaries between different domains, but the distinction is at this stage impracticable. For the same reason, a limited number of the subsequent class BFs ($1° < \theta < 2°$) could also have no correspondence with real features. Again, they cannot be separated from 'real' ones.

- There is an evident positive statistical correlation between average gradient and misorientation value for

automatically defined BFs (Fig. 7). This positive correlation shows the gradient distribution in OC images to have a counterpart in terms of real microstructure and thus the validity of image analysis on orientation contrast imaging (IA-OC) techniques in EBSD analysis. It also gives further evidence of the good adherence of the results from the discussed computer analytical method to reality. Unfortunately the positive correlation, while detectable for averaged data, is very weak if calculated from the raw data, effectively making it of qualitative use only.

- After collection of EBSD data and OC image post processing, during which objects are individually analysed and further subdivided into smaller domains if needed, results clear that two thirds of the crystal domain boundaries had already been identified by the pre-EBSD analysis based on gradients only. This is in good accordance with an estimate of 60% of the total boundaries manually identifiable in a single OC image given in literature (Prior et al., 1996; Trimby, 1998). The remaining one third was not directly detectable in the OC image, but was generated by OC image post-processing, thus resulting in a complete boundary map. This shows that the study of the gradient distribution of a single OC image alone is necessary to further EBSD analysis, but not sufficient for completion. Completion may be achieved using one single OC image after post-processing.
- A manual identification of BFs on an OC image is equally inadequate, as in some instances sharp brightness changes in the OC image do not have a microstructural counterpart, or can be associated only to low misorientation angle features. However, some of the high misorientation BFs do not follow any particularly prominent grey-level gradient-based structure. In those cases manual identification would result in misinterpretation.

7. Conclusion

The application of image analysis techniques applied to OC images has proved highly useful in EBSD analysis of geological samples. If compared with the commonly used manual techniques, the advantages can be listed as follows.

- Perfect reproducibility of results.
- Absence of subjective interpretation.
- Strong reduction of misinterpreted or missing boundaries even with the use of a single OC image.
- Any kind of statistic and geometrical measurement on both boundaries and domains can easily be implemented in the same program and made automatic, thanks to vectorisation of the graphical results. All these data are presented as spreadsheets and linked to the position on the OC image of the crystal domains they describe.

Compared with ACOM techniques, the main reason to consider the IA-OC approach is mostly of time usage

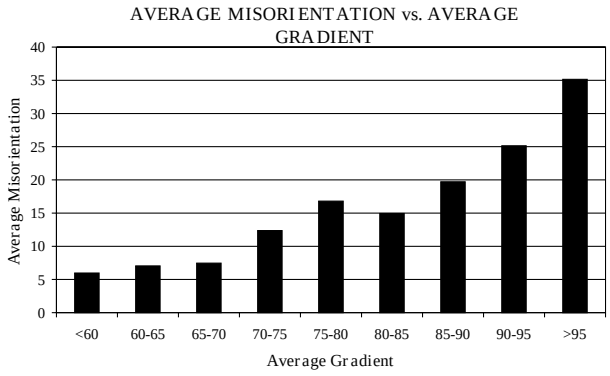

Fig. 7. Histogram showing the positive correlation between BFs classified according to their average gradient and the average misorientation computed for any of the gradient classes. Data refer to post-EBSD BFs coincident with automatically defined BFs (see Fig. 6c).

concern. In ACOM crystal lattice orientation determinations are performed at steps determined by instrumental spatial resolution, while with IA-OC, even if with some redundancy, only positions consistent with the OC image characteristics are considered. For the small area discussed in this contribution, being the instrumental spatial resolution equal to two pixels (0.8 μm), an ACOM analysis would have required 9600 orientation data, while just 468 have been used to obtain results of ACOM quality. If extended to the entire OC image, the figures would become 76 800 data for ACOM and $\sim$3950 for IA-OC. Considering an average of 1 s needed to collect a single orientation datum with automated EBSD techniques (Day, personal communication) this means more than 21 h of continuous SEM usage with ACOM, and slightly more than 1 h with IA-OC (or 7 h to 20 min against if an optimistic 0.3 s per datum is used). If the pseudosymmetry problem is considered and orientation measurements have to be carried out, or at least checked, manually (as happens if EBSD analysis is performed using the currently available CHANNEL + software versions 3.*x* and 4.*x*), all the operational times must be multiplied by a factor 100, making ACOM impractical for low-symmetry materials like quartz. If pseudosymmetry allowed automated interpretation of EBSPs problems are overcome. IA-OC will still require fewer analytical points.

Finally, we are in the process of trying the software onto a range of other images because its outputs of grain boundary lengths and orientations, object centroids, and long/short axes are of wide potential use in other areas of structural geology.

Acknowledgements

We wish to thank Kornelius Veltkamp for his technical support and useful advice on SEM usage. Patrik Trimby has provided the quartz mylonite samples. This work was funded, in part, by NERC grant GR311768. M. Bartozzi's PhD is funded in part by a grant issued by the University of Bologna, Italy, and in part by the University of Liverpool.

References

Adams, B.L., 1997. Orientation imaging microscopy: emerging and future applications. Ultramicroscopy 67, 11–17.

Adams, B.L., Dingley, D.J., Kunze, K., Wright, S.I., 1994. Orientation imaging microscopy: new possibilities for microstructural investigations using automated BKD analysis. In: Bunge, H.J. (Ed.). Textures of Materials (Proc. ICOTOM 10). Materials Science Forum, vols. 157-162, pp. 31–42.

Adams, B.L., Wright, S.I., Kunze, K., 1993. Orientation imaging: the emergence of a new microscopy. Metallurgical Transactions 24A, 819–831.

Day, A., 1993. Developments in the EBSD technique and their application to grain imaging. PhD Thesis, University of Bristol, Bristol, UK.

Goldstein, H., 1980. Classical mechanics. Addison-Wesley Publishing Company, Philippines.

Kunze, K., Heidelbach, F., Wenk, H.-R., Adams, B.L., 1995. Orientation imaging microscopy of calcite rocks. In: Bunge, H.J., Siegesmund, S., Skrotzki, W., Weber, K. (Eds.), Textures of Geological Materials. DGM Informationsgesellschaft MbH, pp. 127–144.

Lloyd, G.E., 1987. Atomic number and crystallographic contrast images with the SEM: a review of backscattered electron techniques. Mineralogical Magazine 51, 3–19.

Newbury, D.E., Joy, D.C., Echlin, P., Fiori, C.E., Goldstein, J.I., 1986. Advanced Scanning Electron Microscopy and X-ray Microanalyses. Plenum Press, New York, London.

Prior, D.J., Trimby, P.W., Weber, U.D., Dingley, D.J., 1996. Orientation contrast imaging of microstructures in rocks using forescatter detectors in the scanning electron microscope. Mineralogical Magazine 60 (403), 859–869.

Prior, D.J., Wheeler, J., 1999. Feldspar fabrics in a greenschist facies albite-rich mylonite from electron backscattered diffraction. Tectonophysics 303, 29–49.

Randle, V., 1992. Microtexture Determination and its Applications. The Institute of Materials, London.

Reimer, L., 1985. Scanning Electron Microscopy—Physics of Image Formation and Microanalysis. Springer-Verlag, Berlin, Heidelberg.

Trimby, P.W., 1998. Quantifying Microstructures—The Development and Application of a New Technique to Quartzitic Shear Zones. PhD Thesis, University of Liverpool, Liverpool, UK.

Trimby, P.W., Prior, D.J., 1999. Microstructural imaging techniques: a comparison between light and scanning electron microscopy. Tectonophysics 303, 71–81.

Wilkinson, A.J., Hirsch, P.B., 1997. Electron diffraction based techniques in scanning electron microscopy of bulk materials. Micron 28 (4), 279–308.